Equation Chapter 1 Section 1 Mobility inference of the Cahn-Hilliard equation

from a model experiment

Zirui Mao^{1†a}, Michael J. Demkowicz^a

^aDepartment of Materials Science and Engineering, Texas A&M University, College Station, Texas 77843,

USA

Abstract: A challenge in phase field modeling of phase-separating binary systems using the Cahn-Hilliard

equation (CHE) is the determination of the mobility coefficient, which controls the kinetics of order parameter

evolution. This work presents numerical simulations to assess the feasibility of determining mobility in the CHE

from a notional, model experiment. The qualitative behavior of these simulations differentiates between a

mobility that is uniform throughout the system and one that is restricted only to phase interfaces. Moreover,

quantitative analysis of the proposed model experiment permits inference of the product of mobility and the

coefficient of the uniform free-energy term as well the characteristic length of the CHE. If the free energy

coefficient is determined by other means (e.g., form thermodynamic or atomistic models), then the mobility may

be calculated, as well.

Keywords: Mobility; Cahn-Hilliard equation; inference; phase field modeling; microstructure evolution.

Introduction

† Correspondence to: Zirui Mao, Department of Materials Science and Engineering, Texas A&M University, College Station, Texas

77843, USA. maozr@tamu.edu

1

The motivation for this work is to advance phase field simulations of microstructure evolution in composites of phase-separating metals. Examples of such composites include laminates made by vapor deposition [1] or roll bonding [2], particulate composites made by ball milling [3] or high pressure torsion [4], and hierarchically-structured composites that self-organize during vapor co-deposition [5]. The microstructures of these composites are relatively stable at room temperature, but change substantially under high temperature annealing. For example, copper (Cu)-niobium (Nb) multilayers pinch off and spheroidize [6], [7], ball-milled composites coarsen and recrystallize [8], and co-deposited alloys phase separate into complex composite structures [9], [10].

Phase field simulations based on the Cahn-Hilliard equation (CHE) [1][2] are well-suited to modeling microstructure evolution in metal composites [13][14] as well as in other phase-separating materials [15]–[18]. Yet direct comparisons of these simulations to experiments remains out of reach because the mobility parameter, M, which governs the kinetics of the CHE, has never been determined for binary systems of phase separating metals. In alloys of mutually-soluble elements, mass transport is dominated by lattice diffusion and mobilities may be computed directly from lattice diffusion mechanisms and thermodynamic data (e.g., as in Al-Zn [19], Cu-Au and Cu-Pt [20], Mo-Ta, Mo-W, Mo-Nb [21], Ti-Sn [22], Co-based alloys [23], Fe-based alloys [24], Ag-Cu and Ag-Pd [25], and Ni-Cu-Ti [26]). However, in composites of phase-separating metals, mass transport occurs predominantly along interfaces between constituent phases. Due to the complexity of interface structures and atomic transport mechanisms [27], there is no viable way to compute M directly from first principles. Indeed, even the form of the mobility parameter—e.g., whether or not it only takes on non-zero values at interfaces—is unknown. In the present work, we propose a model experiment and accompanying

quantitative inference strategy that, taken together, may be used to determine both the form and value of the CHE mobility parameter.

The core idea of the proposed approach is to determine M by matching phase field simulations to experimental observations of microstructure evolution. A similarly-motivated strategy has been adopted by Tavakoli et al., who inferred the mobility in Pb-Sn-a phase-separating binary-from experimentally determined coarsening rates [28]. A drawback of this approach is that it requires large experimental data sets to average out statistical fluctuations in microstructure evolution. Moreover, it does not provide a means of determining whether M is non -zero only at interfaces. Zhao et al. inferred constitutive parameters from a temporal sequence of images taken from phase field simulations [29]. The same group then applied this method to extract thermo-mechanical properties of an aluminum rod in a much-simplified experimental setting [30]. Their approach requires continuous, in situ observation of order parameter evolution in a single sample: a criterion that is difficult to meet in metal composites, where characterization is usually destructive. Hulikal et al. adopted a different strategy in their study on lithiation of electrodes: they inferred the mobility of the CHE directly from galvanostatic and potentiostatic measurements [31]. Their approach is clearly the most robust in a setting where microstructure evolution couples to an externally measurable field or current. However, this is not the case during thermally-assisted microstructure evolution in most metal composites.

The new approach proposed here infers CHE mobility from a notional, model experiment that is, in principle, straightforward to carry out on physical vapor deposited metal composites. We propose a quantitative inference strategy that determines the product of mobility and free energy coefficient as well the characteristic length of the CHE. Provided that the free energy coefficient may be determined by other means (e.g., from

thermodynamic models or atomistic simulations), the mobility coefficient itself may be determined. The experiment relies on a series of isothermal anneals. Thus, the temperature dependence of *M* may be determined by repeating the experiment at different temperatures. Finally, the proposed method distinguishes between uniform mobility and one of the form considered by Cahn et al. [32], which is restricted to take on non-zero values only at phase interfaces.

The Model Experiment

Qualitative description of the model experiment

The proposed model experiment consists of annealing the specially-designed microstructure illustrated in Fig. 1. The microstructure is composed of a layer of metal B embedded in a matrix of another metal, A. The layer of metal B does not span the entire length of the model, but rather terminates along a straight tip, as illustrated in Fig. 1. The length of the layer, L, is much greater than its thickness, H, so that, for all practical purposes, the layer may be considered semi-infinite. The two components, A and B, are considered non-reacting (they do not form compounds) and immiscible (they phase separate with negligible mutual solubility). The only thermodynamic driver for evolution of the model microstructure is capillarity, i.e., reduction of the total energy of the A/B interfaces. As will be shown below, capillarity causes the tip of the terminated layer to become rounded and to retract towards the root of the layer (i.e., to the left, in Fig. 1). Because $L \gg H$, the retraction is not affected by conditions at the root of the layer (i.e., boundary conditions).

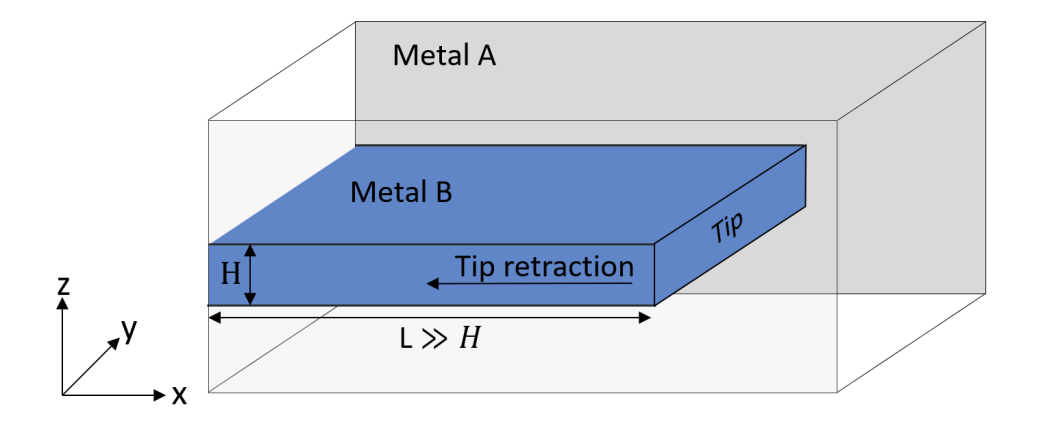


Figure 1: Internal microstructure of the proposed model experiment.

Phase field model of the model experiment

We carried out phase field modeling of the proposed model experiment using the Cahn-Hilliard equation (CHE):

$$\frac{\partial c}{\partial t} = -\nabla \cdot J, \ J = -M(c) \nabla \mu, \ \mu = \frac{\partial F(c)}{\partial c} - \gamma \nabla^2 c \tag{1}$$

Here, $c \in [-1, 1]$ is an order parameter representing the relative concentration difference of the two phases, t is time, J is phase flux, M denotes mobility, μ is chemical potential, g is the gradient energy coefficient, and F(c) is the bulk free energy density. We adopt the double-well potential function

$$F(c) = \Delta F(1 - c^2)^2$$
 (2)

This function has minima at $c = \pm 1$ separated by a barrier of height ΔF . This form of the energy density causes the c field to separate into regions where $c \approx 1$, which we identify with component A, and $c \approx -1$, component B. At boundaries between these regions, c changes smoothly from -1 to 1 over a distance of , which may be considered the characteristic thickness of A/B interfaces in the model. The gradient energy coefficient is taken to be a scalar. Therefore, A/B interfaces have the same characteristic thickness and characteristic energy, , regardless of their orientation.

The mobility coefficient is also taken to be scalar, meaning that there is no constitutive anisotropy of mass transport in our model. We consider two forms of the mobility coefficient. In the first, $M = M_0$ is a constant. We refer to this form as "uniform mobility." In the second, M is a function of the order parameter, c:

$$M(c) = M_0 |1 - c^2|. (3)$$

This form of mobility was proposed by Cahn et al. [32] to model interface-dominated transport: within regions corresponding to components A and B ($_C = \pm 1$), Eqn. 3 predicts M = 0 while at A/B interfaces ($_C = 0$), it gives $M = M_0$. We refer to this form of mobility as "interfacial mobility." For both forms, the mobility factor, M_0 , defines a characteristic time scale, $T^* = \gamma/(M_0 \Delta F^2)$. A description of our approach to solving the CHE and analyzing the results is provided in the Methods section.

Qualitative description of layer retraction in simulation

Fig. 2 shows representative 3-D simulations of layer retraction under uniform mobility (left) and interfacial mobility (right). Animations of both simulations are provided in Supplementary Materials. At short times, the behavior of both models is comparable: the sharp corners of the terminating edge of the layer become rounded and the layer begins to retract. As it retracts, a bulge forms at the terminating edge of the layer. However, at longer times, qualitative differences between the two different models become apparent.

Under uniform mobility, the bulge increases in diameter while remaining connected to the retracting layer at all times. By contrast, under interfacial mobility, the retracting layer begins to form a neck ahead of the bulge, as shown in Fig. 2. This neck eventually pinches off, causing the bulge to detach from the layer. The layer subsequently continues to retract, forming another bulge that also eventually detaches. Thus, layer retraction in

the interfacial mobility case produces a series of cylinders while the uniform case does not. With the exception of the first cylinder, whose size is influenced by the initial conditions of the model, all of these cylinders have identical radius and spacing.

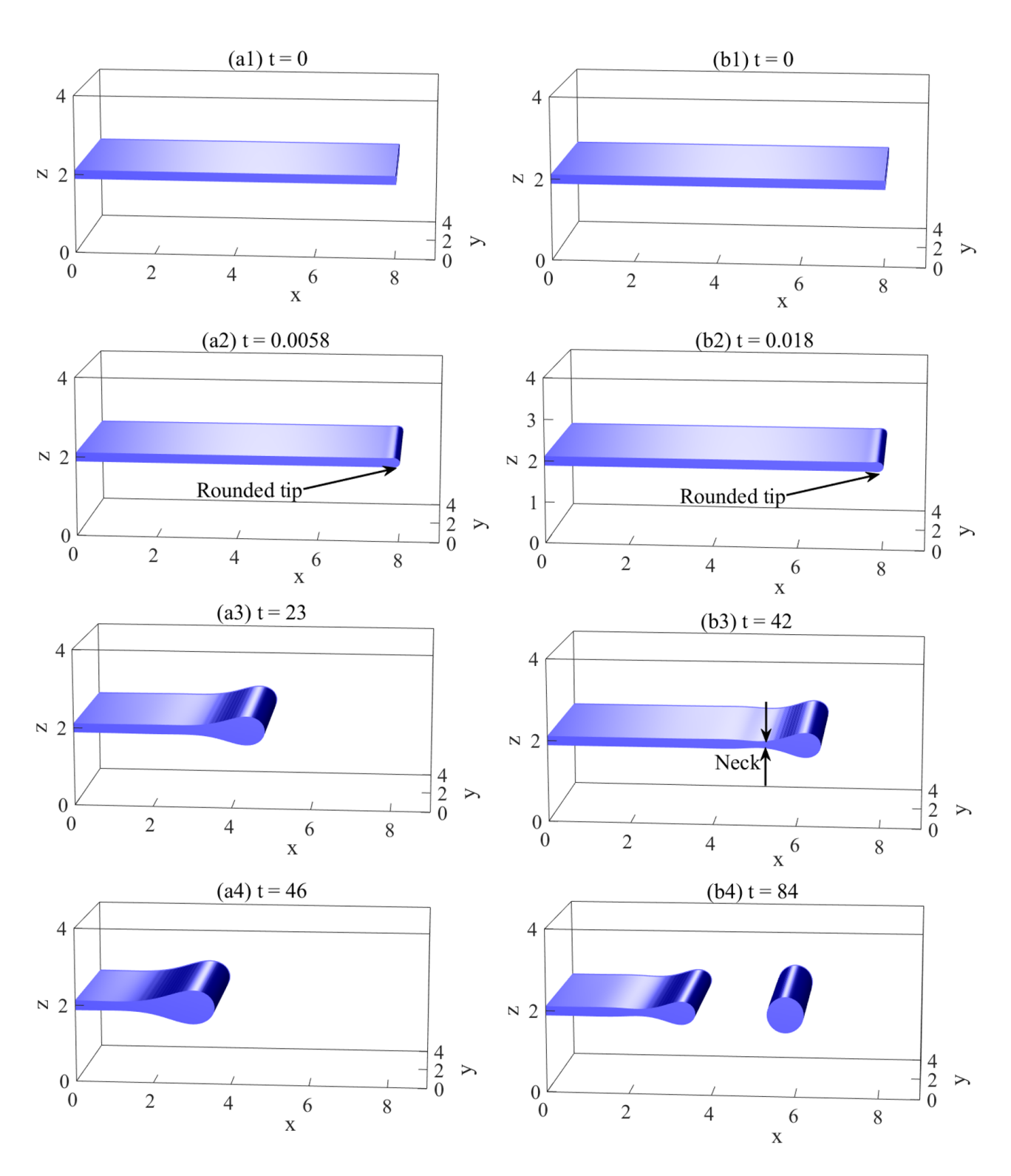
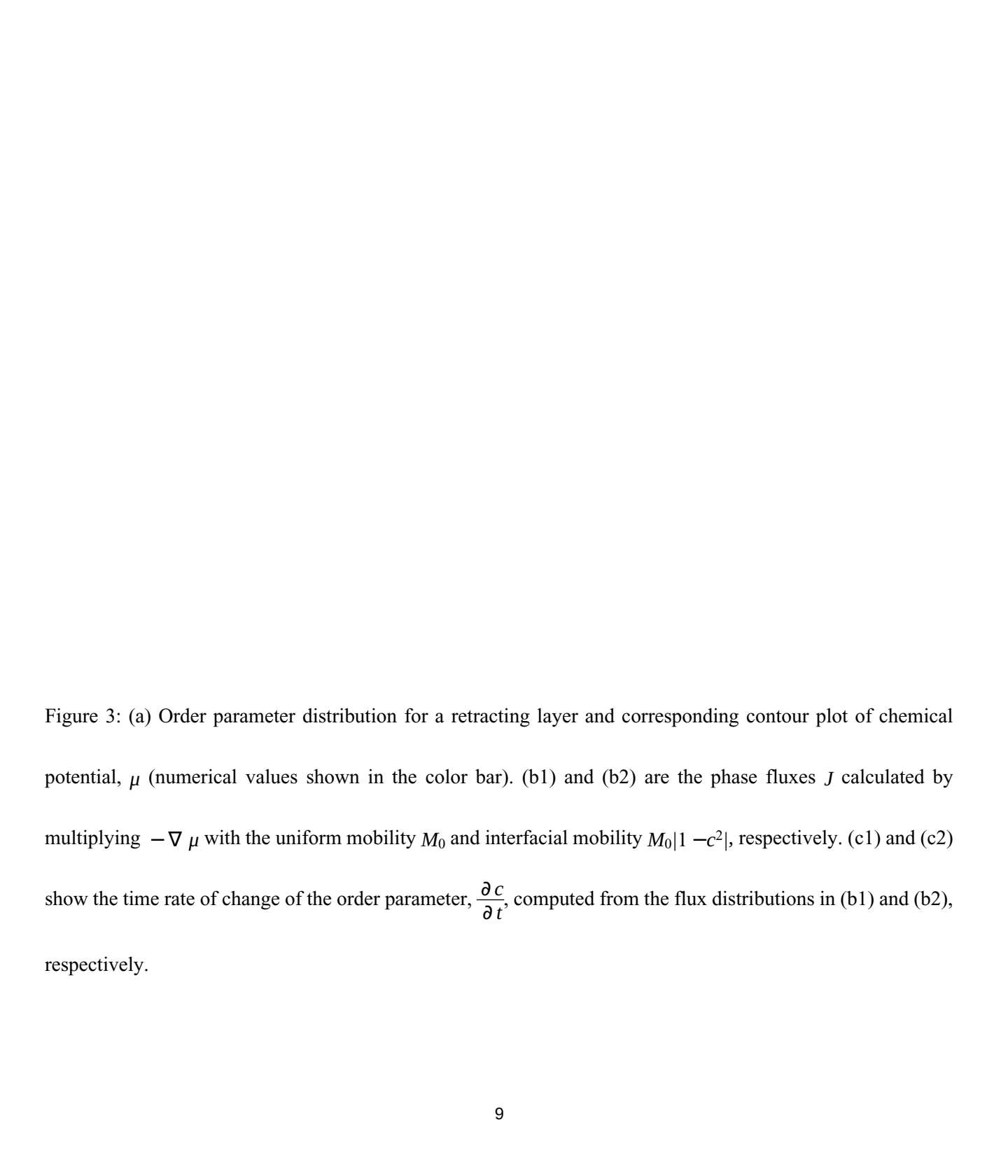


Figure 2: Snapshots of layer retraction at different times under uniform mobility (left) and interfacial mobility (right). Only the layer phase is shown. These simulations use $M_0 = 1$, $\Delta F = 0.25$, $\gamma = 10^{-3}$, and H = 0.2.

The qualitatively different layer retraction behaviors under the two forms of mobility may be explained by differences in the flux distribution between these two cases. Figure 3 illustrates these differences on the example of a single order parameter distribution and its corresponding chemical potential profile, shown in Fig. 3(a). Vector plots of the corresponding phase fluxes, J, under uniform and interfacial mobility are shown in Fig. 3(b1) and 3(b2), respectively. Because the chemical potential gradient in both cases is the same (derived from the order parameter distribution in Fig. 3(a)), the differences between these flux distributions are due entirely to differences in the mobility functions. Figures 3(c1) and 3(c2) shows the time rate of change of the order parameter, $\frac{\partial c}{\partial t}$ (computed as negative the divergence of the flux, J, following Eqn. 1), corresponding to 3(b1) and 3(b2), respectively.



As shown in Fig. 3(b1), there is a phase influx from the matrix into the layer in the region just behind the bulge that forms at the terminated edge. This influx shows that phase transport under uniform mobility is not restricted to the interface and occurs through the phase interiors, as well. However, the influx seen in Fig. 3(b1) is absent in Fig. 3(b2) because the interfacial mobility function, $M_0|1-c^2|$, restricts phase transport to the interfacial region. The consequence of these differences is that, in the case of interfacial mobility, there is an area just behind the bulge that forms at the terminated edge where $\frac{\partial c}{\partial t} < 0$, as shown in Fig. 3(c2). This area is where the neck in the layer initially develops, eventually leading to the pinchoff of the layer. No such region of negative $\frac{\partial c}{\partial t}$ may be found behind the bulge in the uniform mobility case, Fig. 3(c1). Consequently, there is no layer necking or pinchoff, in this case.

To assess the robustness of these findings, we repeated the above-mentioned 3-D simulations with sinusoidal shape perturbations imposed upon the layer along the *y*-axis direction. We find that these perturbations attenuate without altering the sequence of events described in Fig. 2. We also carried out separate simulations on free-standing cylinders under periodic boundary conditions, such as those generated during layer retraction in the interfacial mobility case. As expected, these simulations predict that the cylinders eventually break up into spheres through the Plateau-Rayleigh instability [33], [34] (see Supplementary Materials), albeit over considerably longer times than required for the cylinders to detach from the retracting layer.

The foregoing simulations lead to two important conclusions. First, the form of the mobility parameter—*i.e.*, whether or not it is composition dependent—may be deduced through qualitative inspection of the layer retraction process: breakup of the layer into a series of cylinders signals interfacial mobility of the form shown in

Eqn. 3 while lack of such breakup indicates the mobility is uniform. Second, the layer retraction process for both interfacial and uniform mobilities is quasi-two dimensional: changes in layer morphology within the x-z plane occur much faster than along the y-direction. Thus, to develop strategies for quantitative inference of M_0 , we need only rely on 2-D simulations of layer retraction within cross sections along the x-z plane.

Results

Inference of uniform mobility

Inference strategy

If the layer retracts without forming a series of pinched-off cylinders, we conclude that the mobility does not depend on composition and proceed to infer the numerical value of M_0 through quantitative analysis of layer retraction. Using the definitions of the characteristic quantities, L^* , T^* , and E^* , the mobility coefficient, M_0 , may be expressed as

$$M_0 = \frac{L^{*5}}{F^*T^*}. (4)$$

Our objective is therefore to determine L^* , T^* , and E^* from the layer retraction process and then to compute M_0 from these quantities. We will assume that the only experimentally accessible information is the shape of the retracting layer as a function of time. For example, this shape may be found by imaging a cross-section through a sample, such as that shown in Fig. 1, after annealing for a pre-determined period of time. Notably, we will not assume that the distance by which the layer has retracted can be measured in an experiment. This assumption reflects the difficulty of creating reliable, fixed fiducial markers with respect to which the displacement of the retracting layer may be measured with precision.

While the exact shape of the entire retracting layer is available, in principle, we find that the most convenient aspect of the shape to track during layer retraction is the curvature, κ , of the A/B interface. Specifically, we will track the maximum interface curvature, κ_{max} , which is located invariably at the tip of the retracting layer. As will be shown below, the dependence of κ_{max} on time, t, follows the power law

$$\kappa_{max} = At^u.$$
(5)

Thus, the time dependence of κ_{max} may be characterized by the two fitting constants, A and u. Similar power law dependencies for other quantities have been observed in previous phase field modeling studies [35]–[38].

Our goal is to carry out phase field simulations over a range of L^* , T^* , and E^* values and for multiple layer thicknesses, H, to arrive at functional dependencies, $A = f(L^*, T^*, E^*; H)$ and $u = g(L^*, T^*, E^*; H)$. Provided that A and u depend on all characteristic quantities, L^* , T^* , and E^* , over some range of H values, these functions may be inverted to express L^* , T^* , and E^* as a function of A, u, and H. In this way, the mobility coefficient, M_0 , may be ultimately expressed in terms of A, u, and H, all of which are experimentally accessible.

Dependence of A and u on L^* , T^* , and E^*

No dependence of A or u on E^* . We find that A and u do not depend on E^* . This conclusion may be supported analytically by considering two forms of the CHE: one with parameters M_0 , ΔF_0 , γ_0 and the other with M_0/ϵ , $\epsilon \Delta F_0$, $\epsilon \gamma_0$, where ϵ is any positive number. These two sets of parameters yield different values of E^* , but identical L^* and T^* . Substituting the two sets of parameters back into the CHE predicts identical rates of change of the order parameter with time, $\partial c/\partial t$. Thus, different values of E^* lead to identical time histories of layer

retraction—and therefore identical A and u—provided that L^* and T^* remain unchanged. We verified this conclusion numerically as shown in Fig. 4a.

Dependency of u on (H/L^*) . We use dimensional analysis to identify the most general admissible parametric dependency of u on H, L^* , and T^* [39]. Since the dependent variable, u, is already dimensionless and there is only one dimensionless ratio that may be constructed from the independent variables, namely $\Pi_1 = H/L^*$, we conclude that u cannot depend on T^* . Buckingham's π -theorem [40] then gives $u = g(H/L^*)$. To confirm this deduction, Fig. 4b compares two κ_{max} -t curves with different T^* , but identical H and L^* . When plotted on a logarithmic scale, the fitted slopes at long times yield u. For both curves, the slopes are identical, confirming that u does not depend on T^* .

Dependency of $A \cdot L^*T^{*u}$ on H/L^* . Similarly, for the dependent variable A, the complete set of independent parameters is H, L^* , and T^* . If we pick L^* and T^* as the complete, dimensionally independent subset, the dimensionless, independent variable becomes $\Pi_1 = H/L^*$ and the dimensionless, dependent variable is $\Pi_0 = A \cdot L^*T^{*u}$. Hence, following the Buckingham Π -theorem [40], we get $A \cdot L^*T^{*u} = f(H/L^*)$.

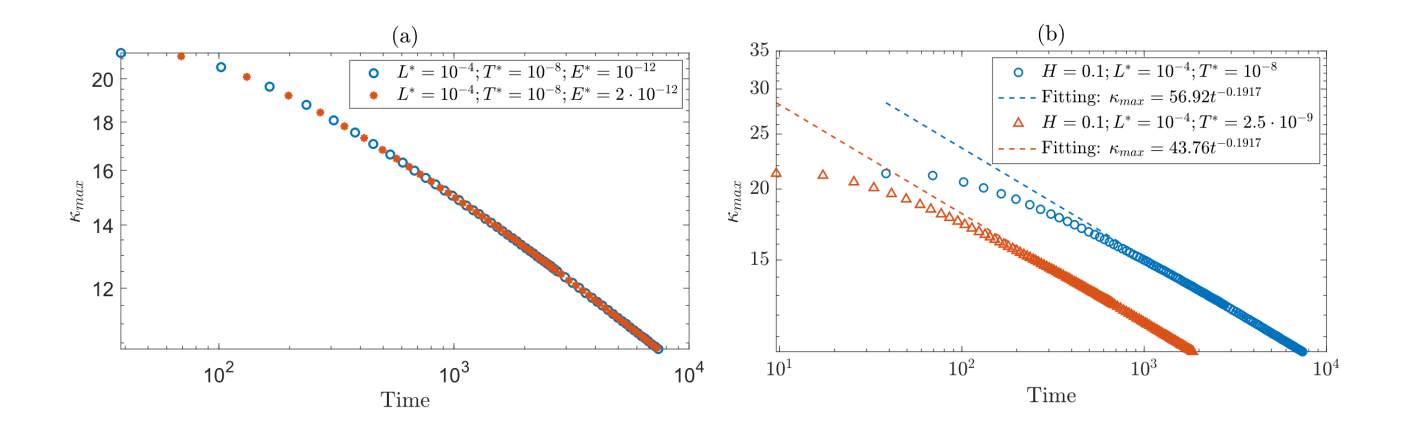


Figure 4: (a) Comparison of κ_{max} -t under different E^* but identical L^* and T^* . In case 1 represented by blue open symbols, $M_0 = 1$, $\Delta F_0 = 1$, $\gamma_0 = 10^{-8}$; in case 2 represented by red stars, $M_0 = 1/2$, $\Delta F_0 = 2$, $\gamma_0 = 2 \cdot 10^{-8}$. (b) Power law fits of maximum curvature ν s. time under identical H and L^* , but different T^* .

Inference of M_0

According to Eqn. (4), M_0 depends on L^* , T^* , and E^* . However, since we have found that A and u show no dependence on E^* , the proposed inference strategy cannot determine M_0 by itself, but rather only the product $M_0E^* = L^{*5}/T^*$. Substituting in the expressions for L^* , T^* , and E^* , this relationship may be further rewritten as $M_0\Delta F = \frac{1}{M^0} = L^{*2}/T^*$, where ΔF is the barrier height in the free energy function shown in Fig. 2. Thus, the proposed model experiment and inference strategy may be used to determine $\frac{1}{M^0}$, which, in turn, may be used to find M_0 , provided that ΔF is determined through other means, as elaborated in the discussion section.

Using the numerical results listed in Table 1 and the parametric dependencies described in the preceding section, we find

$$u = -3.27(\frac{H}{L^*})^{-1} - 0.1884 \tag{6}$$

$$AL^*T^{*u} = 8.2(\frac{H}{L^*})^{-0.54} \tag{7}$$

The quality of these fits is illustrated in Fig. 5. Using these expressions, we write the characteristic variables L^* and T^* in terms of the experimentally measurable quantities, $H_{\rm exp}$, $u_{\rm exp}$, and $A_{\rm exp}$, allowing us to write $\frac{-}{M^0}$ as

(8)

Table 1: Power law fitting results for phase field simulations over a range of H, L^* , and T^* .

	L*	T*	A	и
H				
0.1	5.657 •10 -4	3.2 •10 ⁻⁷	44.82	-0.2068
0.1	4.0 •10 -4	1.6 •10 ⁻⁷	46.34	-0.2013
0.1	2.828 •10 -4	8 •10 ⁻⁸	48.44	-0.1977
0.1	2.0 •10 -4	4 •10 -8	50.85	-0.1949
0.1	1.414 •10 -4	2 •10 -8	54.29	-0.1931
0.1	1.0 •10 -4	1 •10 -8	56.92	-0.1917
0.1	7.071 •10 -5	5 •10 ⁻⁹	60.17	-0.1907
0.1	5.0 •10 ⁻⁵	2.5 •10 -9	63.97	-0.1901
0.1	1.0 •10 -4	5.553 •10 ⁻⁹	50.85	-0.1917
0.2	5.0 •10 -4	2.5 •10 -7	32.05	-0.1965
0.2	2.0 •10 -4	4 •10 -8	37.23	-0.1917

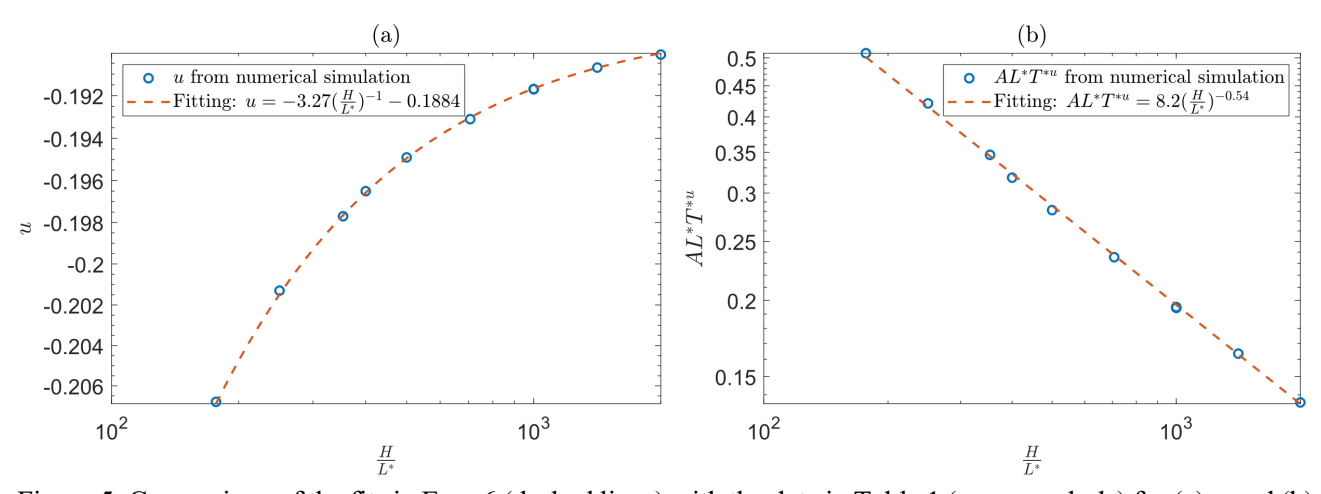


Figure 5: Comparison of the fits in Eqn. 6 (dashed lines) with the data in Table 1 (open symbols) for (a) *u* and (b) *A*.

Inference of interfacial mobility

Inference strategy

If the layer forms a series of pinched-off cylinders while retracting, we conclude that the mobility depends on composition. As in the uniform case, our strategy remains to infer M_0 from Eqn. (4) by determining the characteristic length, time, and energy scales, L^* , T^* , and E^* , from the time-evolution of the shape of the receding layer. However, since the layer retraction process in the interfacial mobility case is qualitatively different from the uniform case, we will not rely on measurements of interface curvature to find L^* , T^* , and E^* . Rather, we will rely on finding the spacing, D, between adjacent pairs of cylinders formed by pinch-off from the retracting layer as well as the average time, Φt , between the pinch-off of successive cylinders. The definitions of D and Φt are illustrated in Fig. 6a.

In the remainder of this subsection, we use phase field modeling to find D and Φt for different combinations of L^* , T^* , E^* , and layer thickness, H, yielding the functional dependencies $D = F(L^*, T^*, E^*; H)$ and $\Delta t = G(L^*, T^*, E^*; H)$. Our goal is to invert these relations, for some range of H, to obtain expressions for L^* , T^* , and E^* in terms of the experimentally measurable quantities, D, Φt , and H. The practical implementation of such measurements is provided in the discussion section.

Dependence of *D* **and** Δt **on** L^* **,** T^* **, and** E^*

No dependence of D and t on E^* . Following the same reasoning presented in the uniform mobility case, we conclude that D and Φt do not depend on E^* . This conclusion is verified with numerical experiments plotted in Fig. 6b.

Dependency of D/L^* on (H/L^*) . The dependent variable D is a function of the independent parameters H, L^* , and T^* . Choosing L^* as the complete, dimensionally independent subset yields the dimensionless, independent

variable $\Pi_1 = H/L^*$ and the dimensionless, dependent variable $\Pi_0 = D/L^*$. Accordingly, we get $D/L^* = F(H/L^*)$. We verified that D is independent of T^* by comparing two simulations with identical L^* and H, but different T^* . Both yield a series of pinched-off cylinders with identical spacing, D as shown in Fig. 6c, as expected.

Dependency of $\bigstar t/T^*$ on H/L^* . The complete set of independent variables determining $\bigstar t$ is H, L^* , and T^* . Choosing L^* and T^* as the complete, dimensionally independent subset, the dimensionless, independent variable is $\Pi_1 = H/L^*$ and the dimensionless, dependent variable $\Pi_0 = \bigstar t/T^*$. Therefore, $\bigstar t/T^* = G(H/L^*)$.

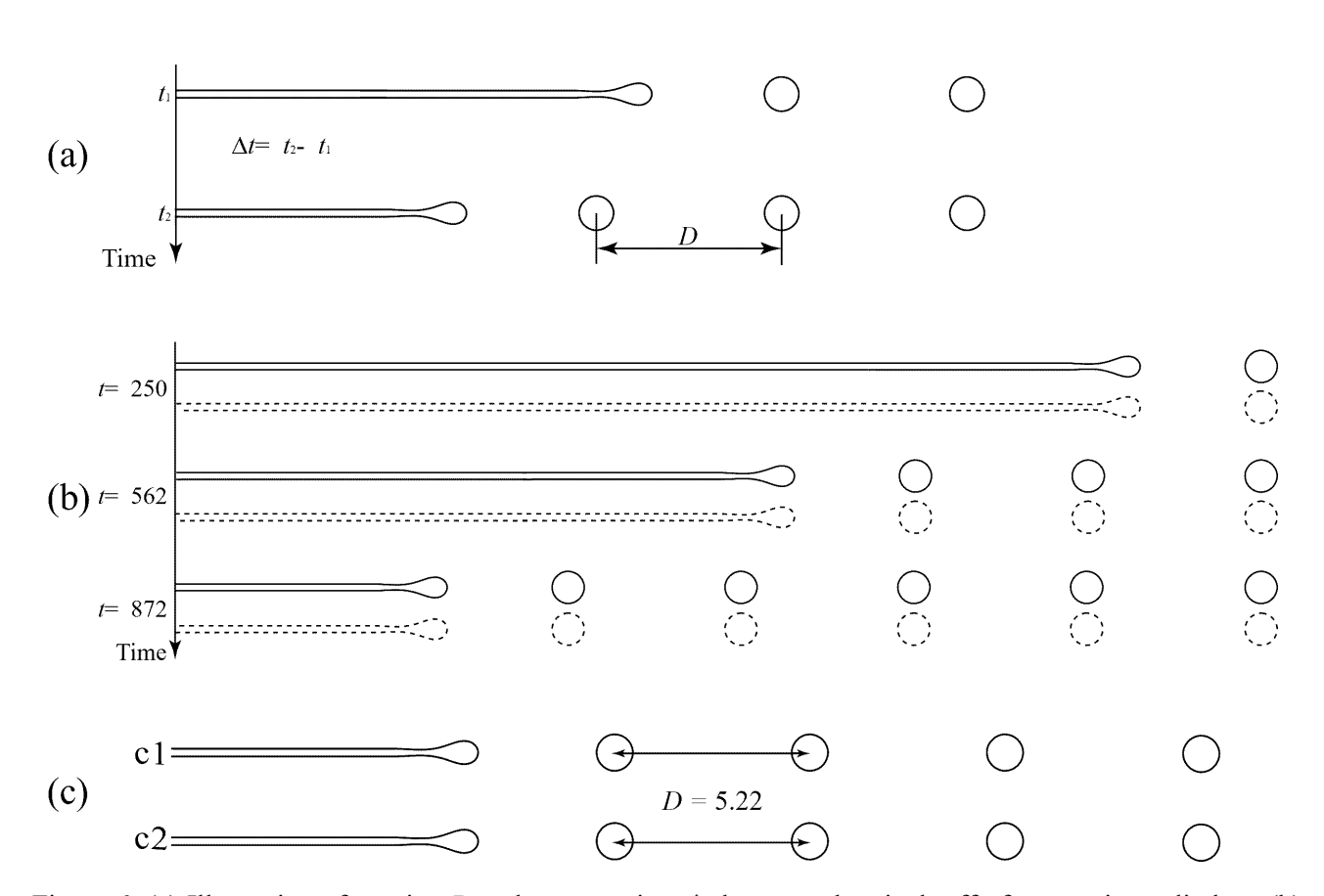


Figure 6: (a) Illustration of spacing D and average time Φt between the pinch-off of successive cylinders, (b) comparison of A/B interface profiles at selected times under different E^* but identical L^* and T^* . The solid profiles have $L^* =$, $T^* = 10^{-3}$, $E^* = 10^{-4.5}$ by employing $M_0 = 1$, $\Delta F = 1$, $\gamma = 10^{-3}$. Dashed profiles have $L^* =$, $T^* = 10^{-3}$, $E^* = 2$ •10^{-4.5} by employing $M_0 = 1/2$, $\Delta F = 2$, $\gamma = 2$ •10⁻³. H = 0.2 in both cases, (c) simulations with $H = 10^{-3}$.

0.2, $L^* =$, and (a) $T^* = 10^{-3}$ (at t = 720) and (b) $T^* = 10^{-4}$ (at t = 72.0).

Inference of M_0

Since D and Φt show no dependence on E^* , we follow the same reasoning as presented in the uniform mobility part to conclude that only the product $M_0 \Delta F = \frac{1}{M^0} = L^{*2}/T^*$ may be inferred from the proposed model experiments. Using the numerical results listed in Table 2 and the parametric dependencies described in the preceding section, we get

$$\frac{D}{L^*} = 0.315(\frac{H}{L^*})^{3.4} \tag{9}$$

$$\frac{\Delta t}{T^*} = 1.5 \cdot 10^{-3} (\frac{H}{L^*})^{10} \tag{10}$$

The quality of these fits is illustrated in Fig. 7. With these relationships, we can express the characteristic variables L^* and T^* in terms of the experimentally measured quantities, H_{exp} , D_{exp} , Φt_{exp} , allowing us to express $-M^0$ as

(11)

Table 2: *D* and Φt from phase field simulations over a range of, *H*, L^* , and T^* .

Н	L^*	<i>T</i> *	D	♠t
0.2		1.0 •10 -3	5.22	156
0.2		1.5 •10 ⁻³	3.22	31.4
		2.0 •10 -3		9.79

0.2		2.30	
0.2	3.0 •10 -3	1.42	1.81
0.2	4.0 •10 -3	1.00	0.590
0.2	1.0 •10 -4	5.22	15.6
0.1	1.0 •10 -3	0.499	0.146
0.1	2.5 •10 -4	2.60	39.5
0.4	4.0 •10 -3	10.5	624

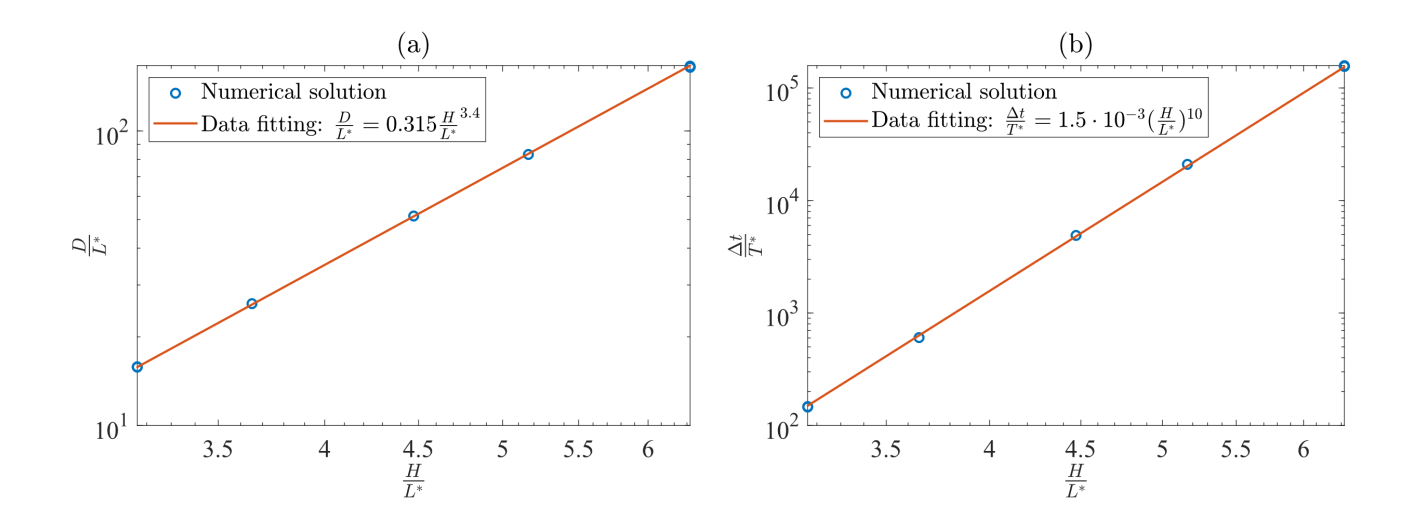


Figure 7: Comparison of the fits in Eqn. (10) (red lines) with the data in Table 2 (open symbols) for (a) D and (b)

♠t.

Conclusions and Discussion

We have proposed a model experiment for determining the mobility term of the Cahn-Hilliard equation, as applied to phase-separating binary systems, and presented an associated inference strategy. The experiment involves tracking the retraction of a semi-infinite layer of one phase embedded in a matrix of the second phase. Qualitative inspection of the retraction process determines whether the mobility is independent of composition or if it depends on composition in such a way that there is non-zero mobility only at the interfaces between the constituent phases: in the latter case, the retracting layer breaks up into a series of disconnected cylinders while in the former case it does not.

This observation is consistent with the findings of Amos *et. al.*, who modeled the spheroidization of a cementite platelet embedded within a ferrite matrix [41]. Their simulation used a mobility matrix defined as composition-weighted average of mobilities of the two phases. In each phase, the mobility was written as the product of a uniform diffusivity with a composition-dependent susceptibility. Thus, similar to our Eqn. 3, their mobility ultimately incorporates a dependence on composition that favors interface transport. They observe that the platelet breaks up into cylinders that further decompose into spheres.

We consider this outcome to be a consequence of the composition-dependence of the mobility used in that study. Indeed, we repeated the simulation of Amos *et. al.* using our phase field model with the interfacial mobility in Eqn. 3 and observed a comparable spheroidization history for the platelet. By contrast, when using a uniform mobility, the platelet simply becomes equiaxed without breaking up. Nevertheless, our conclusions concerning qualitative differences between the uniform mobility and interfacial mobility cases are restricted to the particular potential function (eqn. 2) and gradient energy used in this study (eqn. 1). Indeed, Li et al. observed

the breakup of retracting layers in simulations on phase separating polymer blends that used uniform mobility, but composition-dependent gradient energy coefficient [42].

Quantitative analysis of the layer retraction process in our proposed model experiment permits inference of the product of mobility and uniform free energy density (as defined in Eqn. 2), $\frac{1}{M^0} = M_0 \Delta F$. M_0 cannot be inferred by itself due to the insensitivity of the temporal evolution of the CHE to the characteristic energy, . Indeed, the CHE temporal evolution is completely determined by $\frac{1}{M^0}$ and the scaled gradient coefficient, $\frac{1}{\gamma} = \gamma / \Delta F = L^{*2}$. Our proposed model experiment permits inference of both quantities, with the latter following directly from Eqn. 6 and 9. Thus, a completely parameterized model of microstructure kinetics may be constructed based on these inferences, even if ΔF is unknown. By contrast, Zhao *et al.* claim that their parameter inference method determines all CHE parameters, including E^* [29]. The rationale for this claim is not clear in light of the strict insensitivity of temporal evolution of the CHE to E^* .

The values of M_0 and γ may be computed from M_0 and γ , as inferred by our method, provided that the value of ΔF may be determined by other means. For example, atomistic simulations may be used to compute the energy per unit area, Γ_{AB} , of interfaces between the phases, A and B, that make up the microstructure illustrated in Fig. 1. Such calculations are carried out routinely for composites of phase separating transition metals and typically yield interface energies in the 0.5-1 J/m² range [43], [44]. Following Cahn [45], we write and thereby obtain $\Delta F = \frac{3\Gamma_{AB}}{8L^*}$. Alternatively, ΔF may also be obtained from fits to solubility data, e.g. as in Ref. [46] for the Cu-Nb binary system.

While the work presented here focuses on theoretical and numerical analysis, the proposed model experiment and associated parameter inference are, in principle, straightforward to carry out on phase separating metals, such as Cu-Nb. The microstructure illustrated in Fig. 1 may be synthesized using physical vapor deposition, similar to what has been done previously to synthesize metal multilayer composites [1], [47]. The process would begin with the deposition of a layer of metal A. Next, a physical mask is placed over the sample followed by deposition of a layer of metal B with thickness *H*. Finally, the mask is removed and a second layer of metal A is deposited. This way, a A-B-A trilayer is deposited on parts of the substrate area while the remainder is covered with a single A layer, albeit deposited in two steps. The B layer terminates at the interfaces between areas covered with a A-B-A trilayer and ones with a single A layer.

A sample synthesized as described above may then be annealed isothermally at a prescribed temperature followed by sectioning, e.g. using a focused ion beam [48], along an area perpendicular to the edge of the terminating layer. Inspection of the shape of the retracting layer on this cross section reveals whether or not the layer is breaking up into cylinders and, therefore, whether or not the mobility is composition-dependent, following the form in Eqn. 3. Next, by repeating the isothermal anneal for several samples—all at the same temperature, but for different times—followed by sectioning of all samples, the evolution of the retraction process at successive times is obtained.

For composition independent mobility, the maximum A/B interface curvature is determined for each sample using the fitting procedure described in the "Methods" section, followed by fitting of the power law function in Eqn. 5 to obtain A and u. These values are then substituted into Eqn. 8 to obtain $\frac{1}{M^0}$. For composition dependent

mobility, the values of D and $\clubsuit t$ are determined from direct inspection of the cross sections. One complicating factor in this case is that, for long anneal times, we expect cylinders generated during layer retraction to break up into equiaxed particles via the Plateau-Rayleigh instability [33], [34]. Thus, several sections of each specimen may have to be taken to obtain accurate estimates of the spacing between successive pinch-offs. Alternatively, radiographic characterization perpendicular to the same surface may be employed [49]. Since the latter approach is not destructive, it may obviate the need for multiple samples.

Once D and Φt are known, M^0 is obtained from Eqn. 11. Using standard error propagation methods [50], Eqn. 8 and 11 may also be used to obtain the uncertainty of M^0 from the uncertainties of the experimentally measured variables. For instance, using Eqn. 11, the relative error of M^0 , i.e., δ_M^0/M^0 , is determined as , implying that the mobility coefficient extracted from Eqn. 11 is more sensitive to D than to Δt or H. Similarly, using Eqn. 8, we find , meaning that the sensitivity of the mobility coefficient to experimental parameters depends on the values of these parameters.

Finally, the inference procedure described here makes numerous idealizations of material microstructure. For example, we have ignored the possibility of orientation-dependent interface energies, thermodynamic driving forces for layer retraction arising from elastic misfit or coherency stresses, and pinning effects originating from homophase interfaces (grain boundaries) within the A and B phases. We anticipate that accurate mobility inference may require expansion of our phase field model to account some, if not all, of these factors. A clearer understanding of which—if any—additional factors that must be included is expected to emerge upon comparison of the modeling results presented here to the outcomes of corresponding experiments.

5. Methods

We solve the CHE within the MOOSE framework [51] using the built-in 'SplitCHParsed' kernel and 'Newton' solver. For computational efficiency, adaptive meshing and time-stepping are used. We perform both 3-D simulations, representing the complete microstructure shown in Fig. 1, as well as 2-D simulations, which model a cross-section of the microstructure along the x-z plane. In 2-D simulations, we apply Neumann boundary conditions (BCs) on both c and μ on all boundaries: $\hat{n} \cdot \nabla c = 0$ and $\hat{n} \cdot \nabla \mu = 0$, where \hat{n} is the boundary unit outward normal vector. In 3-D simulations, we also use the same Neumann BCs for all boundaries oriented normal to the x and z axes, as shown in Fig. 1. For boundaries normal to the y axis, we apply periodic BCs. To ensure that model dimensions do not artificially suppress any morphological instabilities of the microstructure, the length of the 3-D models along the y-axis is kept at least 10 times greater than the layer thickness, H.

To obtain the functional dependencies, $A = f(L^*, T^*, E^*; H)$ and $u = g(L^*, T^*, E^*; H)$ in the uniform mobility case, we must compute maximum interface curvatures and fit their time dependence to Eqn. 4. To find κ , we first extract the A/B interface profile, defined as the set of locations where c = 0. Next, using the coordinates of points along the interface, we compute local curvature using the MATLAB code by Mjaavatten [52]. The output is then smoothed using the Gaussian-weighted moving average filter, as implemented in the 'smoothdata' function in MATLAB. The maximum curvature—found invariably at the tip of the retracting layer—is then extracted. This process is repeated at multiple times throughout a layer retraction simulation, yielding a plot of κ_{max} vs. t. Fig. 8a -8c provides an illustrative example of the aforementioned calculations.

To fit the expression in Eqn. 4 to K_{max} vs. t data, we must determine the time range, $[t_{min}, t_{max}]$, over which the fit is to be performed. Our choice of t_{max} and t_{min} is driven by the need to avoid artifacts associated with boundary and initial conditions of the phase field simulations. Fig. 8(d) shows the layer thickness and interface curvature at the root of the retracting layer—i.e., along the left boundary of the model—as a function of time. We see that both quantities are independent of time until a characteristic t_{max} , which is the time when the bulge at the tip of the layer begins to interact with the boundary. We take this t_{max} as the upper bound of the time interval over which the fit is to be performed. Once t_{max} is known, we then consider a range of possible t_{min} values, from zero to t_{max} , and check how the fitted t_{min} and t_{min} depend on the choice of t_{min} . We find that t_{min} are independent of t_{min} , provided that t_{min} is above a threshold value, as illustrated in Fig. 8(e). Below this threshold value, the fitted t_{min} and t_{min} are affected by the initial state of the model, in which the terminated edge of the layer has sharp corners. We therefore choose the threshold value above which t_{min} and t_{min} as the lower bound of our fitting interval. The interval t_{min} is determined separately for each phase field simulation.

Figure 8: Illustrative example of interface curvature calculation: (a) identification of interface location, (b) curvature calculated as a function of location along the interface, and (c) time history of maximum curvature for a simulation with $M_0 = 1$, $\Delta F = 1$, and $\gamma = 3.2 \cdot 10^{-7}$, (d) determination of t_{max} , and (e) determination of t_{min} employed in data fitting.

Availability of data and materials

The animations supporting the conclusions of this article are included in Supplementary Materials.

Acknowledgements

This work was supported by the NSF CDS&E program under grant number 1802867. Computational resources were provided by the High Performance Research Computing (HPRC) center at Texas A&M University. We are grateful to K. Ankit for his early contribution to the development of the mobility inference concept and to K. Ahmed for assistance with the MOOSE software package.

Conflict of interest statement

On behalf of all authors, the corresponding author states that there is no conflict of interest.

References

- ADDIN Mendeley Bibliography CSL_BIBLIOGRAPHY [1] T. E. Mitchell, Y. C. Lu, A. J. G. Jr., M. Nastasi, and H. Kung, "Structure and Mechanical Properties of Copper/Niobium Multilayers," *J. Am. Ceram. Soc.*, vol. 80, no. 7, pp. 1673–1676, Jan. 1997, doi: 10.1111/j.1151-2916.1997.tb03037.x.
- [2] J. S. Carpenter, S. C. Vogel, J. E. Ledonne, D. L. Hammon, I. J. Beyerlein, and N. A. Mara, "Bulk texture evolution of Cu-Nb nanolamellar composites during accumulative roll bonding," *Acta Mater.*, vol. 60, no. 4, pp. 1576–1586, Feb. 2012, doi: 10.1016/j.actamat.2011.11.045.
- S. Zghal, M. J. Hÿtch, J. P. Chevalier, R. Twesten, F. Wu, and P. Bellon, "Electron microscopy nanoscale characterization of ball-milled Cu-Ag powders. Part I: Solid solution synthesized by cryomilling," *Acta Mater.*, vol. 50, no. 19, pp. 4695–4709, Nov. 2002, doi: 10.1016/S1359-6454(02)00285-9.
- [4] M. Wang, R. S. Averback, P. Bellon, and S. Dillon, "Chemical mixing and self-organization of Nb precipitates in Cu during severe plastic deformation," *Acta Mater.*, vol. 62, no. 1, pp. 276–285, Jan. 2014, doi: 10.1016/j.actamat.2013.10.009.
- [5] B. Derby, Y. Cui, J. Baldwin, R. Arróyave, M. J. Demkowicz, and A. Misra, "Processing of novel pseudomorphic Cu-Mo hierarchies in thin films," *Mater. Res. Lett.*, vol. 7, no. 1, pp. 1–11, Jan. 2019, doi: 10.1080/21663831.2018.1546237.

- [6] A. Misra and R. G. Hoagland, "Effects of elevated temperature annealing on the structure and hardness of copper/niobium nanolayered films," *J. Mater. Res.*, vol. 20, no. 8, pp. 2046–2054, Aug. 2005, doi: 10.1557/JMR.2005.0250.
- [7] S. Zheng, J. S. Carpenter, J. Wang, N. A. Mara, and I. J. Beyerlein, "An interface facet driven Rayleigh instability in high-aspect-ratio bimetallic nanolayered composites," *Appl. Phys. Lett.*, vol. 105, no. 11, p. 111901, Sep. 2014, doi: 10.1063/1.4895560.
- [8] S. Zghal, R. Twesten, F. Wu, and P. Bellon, "Electron microscopy nanoscale characterization of ball milled Cu-Ag powders. Part II: Nanocomposites synthesized by elevated temperature milling or annealing," *Acta Mater.*, vol. 50, no. 19, pp. 4711–4726, Nov. 2002, doi: 10.1016/S1359-6454(02)00286-0.
- [9] F. T. N. Vüllers and R. Spolenak, "From solid solutions to fully phase separated interpenetrating networks in sputter deposited 'immiscible' W-Cu thin films," *Acta Mater.*, vol. 99, pp. 213–227, Aug. 2015, doi: 10.1016/j.actamat.2015.07.050.
- [10] B. Derby, Y. Cui, J. K. Baldwin, and A. Misra, "Effects of substrate temperature and deposition rate on the phase separated morphology of co-sputtered, Cu-Mo thin films," *Thin Solid Films*, vol. 647, pp. 50–56, Feb. 2018, doi: 10.1016/j.tsf.2017.12.013.
- [11] J. W. Cahn and J. E. Hilliard, "Free energy of a nonuniform system. I. Interfacial free energy," *J. Chem. Phys.*, vol. 28, no. 2, pp. 258–267, Feb. 1958, doi: 10.1063/1.1744102.

- [12] L.-Q. Chen, "Phase-Field Models for Microstructure Evolution," *Annu. Rev. Mater. Res.*, vol. 32, no. 1, pp. 113–140, Aug. 2002, doi: 10.1146/annurev.matsci.32.112001.132041.
- [13] K. Ankit, B. Derby, R. Raghavan, A. Misra, and M. J. Demkowicz, "3-D phase-field simulations of self-organized composite morphologies in physical vapor deposited phase-separating binary alloys," *J. Appl. Phys.*, vol. 126, no. 7, p. 075306, Aug. 2019, doi: 10.1063/1.5110410.
- [14] Y. Lu, C. Wang, Y. Gao, R. Shi, X. Liu, and Y. Wang, "Microstructure map for self-organized phase separation during film deposition," *Phys. Rev. Lett.*, vol. 109, no. 8, p. 086101, Aug. 2012, doi: 10.1103/PhysRevLett.109.086101.
- [15] J. D. Gunton, R. Toral, and A. Chakrabarti, "Numerical Studies of Phase Separation in Models of Binary Alloys and Polymer Blends," *Phys. Scr.*, vol. 33, pp. 12–19, 1990.
- [16] R. Kenzler *et al.*, "Phase separation in confined geometries: Solving the Cahn-Hilliard equation with generic boundary conditions," *Comput. Phys. Commun.*, vol. 133, no. 2–3, pp. 139–157, Jan. 2001, doi: 10.1016/S0010-4655(00)00159-4.
- [17] D. Anders and K. Weinberg, "Numerical simulation of diffusion induced phase separation and coarsening in binary alloys," in *Computational Materials Science*, 2011, vol. 50, no. 4, pp. 1359–1364, doi: 10.1016/j.commatsci.2010.03.030.

- [18] D. Lu, M. S. Osman, M. M. A. Khater, R. A. M. Attia, and D. Baleanu, "Analytical and numerical simulations for the kinetics of phase separation in iron (Fe-Cr-X (X=Mo,Cu)) based on ternary alloys," *Phys. A Stat. Mech. its Appl.*, vol. 537, p. 122634, Jan. 2020, doi: 10.1016/j.physa.2019.122634.
- [19] Y. W. Cui, K. Oikawa, R. Kainuma, and K. Ishida, "Study of Diffusion Mobility of Al-Zn Solid Solution," doi: 10.1361/154770306X116261.
- [20] Y. Liu, L. Zhang, and D. Yu, "Diffusion mobilities in fcc Cu-Au and fcc Cu-Pt alloys," *J. Phase Equilibria Diffus.*, vol. 30, no. 2, pp. 136–145, Apr. 2009, doi: 10.1007/s11669-009-9469-2.
- [21] Y. Liu, Z. Long, Y. Du, G. Sheng, J. Wang, and L. Zhang, "Diffusion characteristics and atomic mobilities for bcc refractory Mo-Ta, Mo-W, and Mo-Nb alloys," *Calphad Comput. Coupling Phase Diagrams Thermochem.*, vol. 36, pp. 110–117, Mar. 2012, doi: 10.1016/j.calphad.2011.12.004.
- [22] J. L. Wang *et al.*, "Computational Study of Mobilities and Diffusion in Ti-Sn Alloy," *J. Phase Equilibria Diffus.*, vol. 36, no. 3, pp. 248–253, Jun. 2015, doi: 10.1007/s11669-015-0377-3.
- [23] Y. Liu, D. Liang, Y. Du, L. Zhang, and D. Yu, "Mobilities and diffusivities in fcc Co-X (X=Ag, Au, Cu, Pd and Pt) alloys," *Calphad Comput. Coupling Phase Diagrams Thermochem.*, vol. 33, no. 4, pp. 695–703, Dec. 2009, doi: 10.1016/j.calphad.2009.09.001.

- [24] Y. Liu, J. Wang, Y. Du, L. Zhang, and D. Liang, "Mobilities and diffusivities in fcc Fe-X (X = Ag, Au, Cu, Pd and Pt) alloys," *Calphad Comput. Coupling Phase Diagrams Thermochem.*, vol. 34, no. 3, pp. 253–262, Sep. 2010, doi: 10.1016/j.calphad.2010.04.002.
- [25] C. P. Wang, L. N. Yan, J. J. Han, and X. J. Liu, "Diffusion mobilities in the fcc Ag-Cu and Ag-Pd alloys," *Calphad Comput. Coupling Phase Diagrams Thermochem.*, vol. 37, pp. 57–64, Jun. 2012, doi: 10.1016/j.calphad.2012.01.001.
- [26] C. Li, S. Huang, and Y. Liu, "Simulation of atomic mobilities, interdiffusivities and diffusional evolution in fcc Ni-Cu-Ti alloys," *J. Alloys Compd.*, vol. 780, pp. 293–298, Apr. 2019, doi: 10.1016/j.jallcom.2018.10.251.
- [27] K. Kolluri and M. J. Demkowicz, "Formation, migration, and clustering of delocalized vacancies and interstitials at a solid-state semicoherent interface," *Phys. Rev. B Condens. Matter Mater. Phys.*, vol. 85, no. 20, p. 205416, May 2012, doi: 10.1103/PhysRevB.85.205416.
- [28] M. M. Tavakoli, R. Tavakoli, P. Davami, and H. Aashuri, "A quantitative approach to study solid state phase coarsening in solder alloys using combined phase-field modeling and experimental observation," *J. Comput. Electron.*, vol. 13, no. 2, pp. 425–431, 2014, doi: 10.1007/s10825-013-0551-y.
- [29] H. Zhao, B. D. Storey, R. D. Braatz, and M. Z. Bazant, "Learning the Physics of Pattern Formation from Images," *Phys. Rev. Lett.*, vol. 124, no. 6, p. 060201, Feb. 2020, doi: 10.1103/PhysRevLett.124.060201.

- [30] A. L. Cottrill, R. Goulet, F. Fremy, J. Meulemans, M. R. Sheldon, and M. Z. Bazant, "Simultaneous inversion of optical and infra-red image data to determine thermo-mechanical properties of thermally conductive solid materials," *Int. J. Heat Mass Transf.*, vol. 163, p. 120445, Dec. 2020, doi: 10.1016/j.ijheatmasstransfer.2020.120445.
- [31] S. Hulikal, C.-H. Chen, E. Chason, and A. Bower, "Experimental Calibration of a Cahn-Hilliard Phase -Field Model for Phase Transformations in Li-Sn Electrodes," *J. Electrochem. Soc.*, vol. 163, no. 13, pp. A2647–A2659, Sep. 2016, doi: 10.1149/2.0701613jes.
- [32] J. W. Cahn, C. M. Elliott, and A. Novick-Cohen, "The Cahn-Hilliard equation with a concentration dependent mobility: Motion by minus the Laplacian of the mean curvature," *Eur. J. Appl. Math.*, vol. 7, no. 3, pp. 287–301, 1996, doi: 10.1017/s0956792500002369.
- J. Plateau, "Statique expérimentale et théorique des Liquides soumis aux seules Forces moléculaires," in Experimental and theoretical statics of liquids subject to only molecular forces, vol. 2, Paris, France, 1873, p. 261.
- [34] Lord Rayleigh, "On the instability of jets," *Proc. London Math. Soc.*, vol. s1-10, no. 1, pp. 4–13, Nov. 1878, doi: 10.1112/plms/s1-10.1.4.
- [35] G. Sheng, "Coarsening Kinetics of a Two Phase Mixture with Highly Disparate Diffusion Mobility," *Commun. Comput. Phys.*, vol. 8, no. 2, pp. 249–264, Jun. 2010, doi: 10.4208/cicp.160709.041109a.

- [36] J. Zhu, L. Q. Chen, J. Shen, and V. Tikare, "Coarsening kinetics from a variable-mobility cahn-hilliard equation: Application of a semi-implicit fourier spectral method," *Phys. Rev. E Stat. Physics*, *Plasmas, Fluids, Relat. Interdiscip. Top.*, vol. 60, no. 4, pp. 3564–3572, Oct. 1999, doi: 10.1103/PhysRevE.60.3564.
- [37] S. Puri, A. J. Bray, and J. L. Lebowitz, "Phase-separation kinetics in a model with order-parameter-dependent mobility," *Phys. Rev. E Stat. Physics, Plasmas, Fluids, Relat. Interdiscip. Top.*, vol. 56, no. 1, pp. 758–765, Jul. 1997, doi: 10.1103/PhysRevE.56.758.
- [38] L. Guangjin, X. Wenjun, L. Lanzhou, and L. Jianxue, "Phase separation dynamics in binary systems containing mobile particles with variable Brownian motion," *Pramana J. Phys.*, vol. 91, no. 4, p. 55, Oct. 2018, doi: 10.1007/s12043-018-1625-y.
- [39] A. A. Sonin, The Physical Basis of Dimensional Analysis, 2nd editio. Cambridge: MIT, 2001.
- [40] J. Bertrand, "Sur l'homogénéité dans les formules de physique," *Comptes Rendus*, vol. 86, no. 15, pp. 916–920, 1878.
- [41] P. G. K. Amos, A. Bhattacharya, B. Nestler, and K. Ankit, "Mechanisms of pearlite spheroidization: Insights from 3D phase-field simulations," *Acta Mater.*, vol. 161, pp. 400–411, Dec. 2018, doi: 10.1016/j.actamat.2018.09.043.

- [42] Y. C. Li, R. P. Shi, C. P. Wang, X. J. Liu, and Y. Wang, "Predicting microstructures in polymer blends under two-step quench in two-dimensional space," *Phys. Rev. E Stat. Nonlinear, Soft Matter Phys.*, vol. 83, no. 4, p. 041502, Apr. 2011, doi: 10.1103/PhysRevE.83.041502.
- [43] I. J. Beyerlein, J. R. Mayeur, S. Zheng, N. A. Mara, J. Wang, and A. Misra, "Emergence of stable interfaces under extreme plastic deformation," *Proc. Natl. Acad. Sci. U. S. A.*, vol. 111, no. 12, pp. 4386–4390, Mar. 2014, doi: 10.1073/pnas.1319436111.
- [44] M. J. Demkowicz and L. Thilly, "Structure, shear resistance and interaction with point defects of interfaces in Cu-Nb nanocomposites synthesized by severe plastic deformation," *Acta Mater.*, vol. 59, no. 20, pp. 7744–7756, Dec. 2011, doi: 10.1016/j.actamat.2011.09.004.
- [45] J. W. Cahn, "Critical point wetting," J. Chem. Phys., vol. 66, no. 8, pp. 3667–3672, Apr. 1977, doi: 10.1063/1.434402.
- [46] L. Kaufman, "Coupled phase diagrams and thermochemical data for transition metal binary systems-III," *Calphad*, vol. 2, no. 2, pp. 117–146, Jan. 1978, doi: 10.1016/0364-5916(78)90031-7.
- [47] D. Chen, N. Li, D. Yuryev, J. K. Baldwin, Y. Wang, and M. J. Demkowicz, "Self-organization of helium precipitates into elongated channels within metal nanolayers," *Sci. Adv.*, vol. 3, no. 11, p. eaao2710, Nov. 2017, doi: 10.1126/sciadv.aao2710.

- [48] I. McCue, S. Xiang, K. Xie, and M. J. Demkowicz, "The Effect of Microstructure Morphology on Indentation Response of Ta/Ti Nanocomposite Thin Films," *Metall. Mater. Trans. A Phys. Metall. Mater. Sci.*, vol. 51, no. 11, pp. 5677–5690, Nov. 2020, doi: 10.1007/s11661-020-05969-w.
- [49] D. A. Shapiro *et al.*, "Chemical composition mapping with nanometre resolution by soft X-ray microscopy," *Nat. Photonics*, vol. 8, no. 10, pp. 765–769, Jan. 2014, doi: 10.1038/nphoton.2014.207.
- [50] "Propagation of Error." [Online]. Available: https://chem.libretexts.org/@go/page/353. [Accessed: 05-May-2021].
- [51] C. J. Permann *et al.*, "MOOSE: Enabling Massively Parallel Multiphysics Simulation," *SoftwareX*, vol. 11, Nov. 2019, doi: 10.1016/j.softx.2020.100430.
- [52] A. Mjaavatten, "Curvature of a 2D or 3D curve.
 (https://www.mathworks.com/matlabcentral/fileexchange/69452-curvature-of-a-2d-or-3d-curve),
 MATLAB Central File Exchange. Retrieved July 1, 2020." 2020.